ACSNANO

www.acsnano.org

ARTICLE

Ultrasound-Guided Cytosolic Protein Delivery *via* Transient Fluorous Masks

Janna N. Sloand, Theodore T. Nguyen, Scott A. Zinck, Erik C. Cook, Tawanda J. Zimudzi, Scott A. Showalter, Adam B. Glick, Julianna C. Simon, and Scott H. Medina*

Cite This: *ACS Nano* 2020, 14, 4061−4073

Read Online

ACCESS | Metrics & More | Article Recommendations | Supporting Information

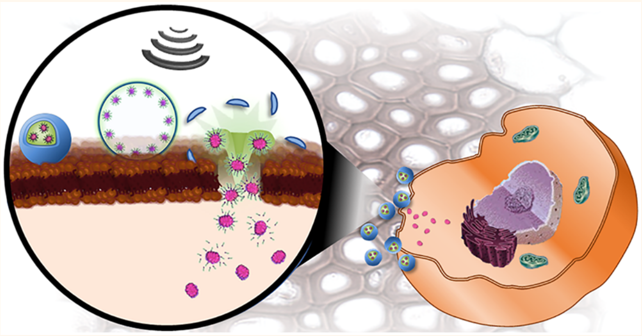

ABSTRACT: **The inability to spatiotemporally guide proteins in tissues and efficiently deliver them into cells remains a key barrier to realizing their full potential in precision medicine. Here, we report ultrasound-sensitive fluoro-protein nanoemulsions which can be acoustically tracked, guided, and activated for on-demand cytosolic delivery of proteins, including antibodies, using clinically relevant diagnostic ultrasound. This advance is accessed through the discovery of a family of fluorous tags, or FTags, that transiently mask proteins to mediate their efficient dispersion into ultrasound-sensitive liquid perfluorocarbons, a phenomenon akin to dissolving an egg in liquid Teflon. We identify the biochemical basis for protein fluorous masking and confirm FTag coatings are shed during delivery, without disrupting the protein structure or function. Harnessing the ultrasound sensitivity of fluorous emulsions, real-time imaging is used to simultaneously monitor and activate FTag−protein complexes to enable controlled cytosolic antibody delivery *in vitro* and *in vivo*. These findings may advance the development of image-guided, protein-based biosensing and therapeutic modalities.**

KEYWORDS: *protein delivery, ultrasound, perfluorocarbon, nanodroplets, theranostics*

Protein biotherapeutics are some of the most potent and selective tools in precision medicine. Drug discovery efforts over the past two decades have yielded an array of therapeutic proteins, particularly monoclonal antibodies, that have transformed the treatment of cancer, autoimmune disorders, and infectious diseases.[1] However, to date, all clinically approved protein therapeutics are restricted to ligands present in the extracellular milieu or disease targets displayed at the cell surface. This is a consequence of their large size and hydrophilic nature, which prevents the efficient transport of proteins across the lipid cell membrane.[1,2] Proteins that bind intracellular targets to modulate signal transduction and gene regulation pathways represent an untapped wealth of therapeutics that could advance precision medicine if delivered properly.

Accordingly, efficient and precise transduction of proteins across the membrane and into the cytoplasm of target cells remains a significant challenge.[3] Clinically relevant approaches have largely employed lipid-,[4−6] polymer-,[7−9] graphene-,[10−12] or gold-based[13,14] nanocarriers. Polymeric scaffolds are particularly attractive vehicles due to their efficient cellular uptake, facile protein complexation methods, and an ability to integrate biodegradable and stimuli-responsive constituents.[15,16] To deliver the protein payload, these delivery platforms are often functionalized or modified to bind to the cell surface to enable their endocytic uptake. Although this approach improves stability and tissue-specific localization of loaded proteins, a key translational hurdle is endosomal sequestration and degradation of the sensitive biologic cargo following uptake.[2,3,16] More importantly, these inert nanocarriers cannot be actively monitored or guided once administered, leading to poor protein transduction efficiencies in the target tissue and off-target effects.

Perfluorocarbon (PFC) nanoemulsions are an emerging class of carriers with medical applications that span synthetic blood substitutes,[17,18] ischemic tissue oxygenation,[19−21] embolotherapy,[22,23] and, more recently, stimuli-responsive delivery devices.[24−27] The weak intermolecular forces that

Received: November 5, 2019
Accepted: March 5, 2020
Published: March 5, 2020

result from the low polarizability of fluorines, as well as the strong intramolecular C−F bond, impart PFCs with unusual physicochemical properties.[28] One particularly attractive property is the ability of PFCs to undergo liquid−gas phase transitions in response to ultrasound (US),[29,30] accelerating interest in developing these materials as imaging-guided delivery vehicles.[24−27] However, a key hurdle in the development of PFC nanoemulsions as clinically useful delivery devices is the solubility barrier presented by their fluorous liquid interior.[31] Although a prerequisite for their phase-changing behavior, the fluorinated core often leads to meager, or altogether nonexistent, encapsulation of small molecule drugs and biologics. As a result, loading strategies for PFC carriers have been restricted to double emulsion techniques or surface functionalization.[32−37] This is important as the method of loading has significant implications on cargo stability and mechanisms of payload delivery.[38] For example, harsh physical agitation of double emulsion techniques can denature and inactivate loaded biologics, whereas surface-mediated attachment is challenged by inefficient cargo release, nonspecific delivery to tissue interstitium, and variable biologic outcomes.[24,32,39,40] Importantly, neither of these strategies are capable of direct and efficient transmembrane protein delivery.

Here, we report a paradigm of loading proteins, including immunoglobulins, into the fluorous interior of PFC nanoemulsions to enable their US-mediated cytosolic transduction into cells with spatiotemporal control (Figure 1). This is achieved using a family of fluoro-amphiphilic chemical tags, or FTags, which possess a capacity for fluorous masking. That is, they enjoy a counterbalance of polarity and fluorine content that imparts the ability to transiently associate with proteins and mediate their efficient dispersion within fluorous media *via* favored fluorine−fluorine interactions, all while maintaining the protein's folded and bioactive state. Complementary biophysical techniques elucidate the biochemical basis of this association and demonstrate that fluorinated protein complexes can be loaded into the interior of PFC nanoemulsions and delivered following US vaporization at the cell surface *in vitro* and *in vivo*. Importantly, this approach leverages noninvasive diagnostic US modalities routinely used in the clinic to permit real-time guidance of protein-loaded fluorous nanoemulsions in tissue analogues and to monitor cargo delivery in a temporally precise and quantitative manner.

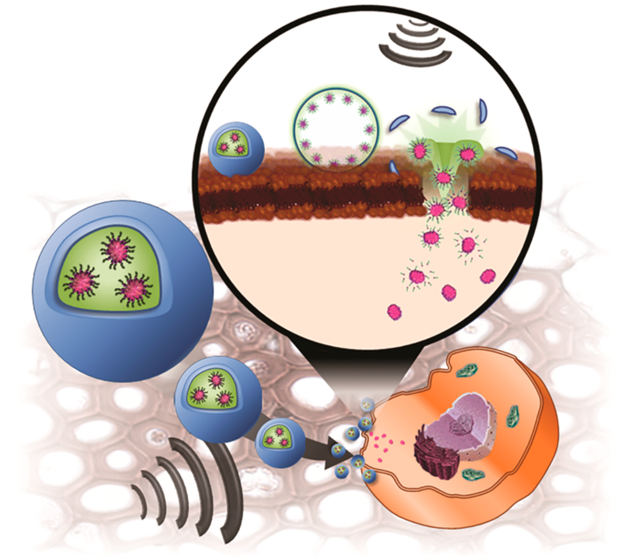

Figure 1. Ultrasound-guided cytosolic delivery of fluorous masked proteins. Acoustically sensitive fluorous nanoemulsions are prepared *via* an amphiphilic emulsifier (blue) that assembles at the surface of a PFC nanodroplet (green), containing the masked protein cargo (pink). Diagnostic US is used to guide the particles in real-time and synchronously trigger particle activation at the cell surface to provide on-demand protein delivery. Here, acoustic vaporization of the liquid nanoemulsion produces a gaseous microbubble that, upon collapse, transiently permeabilizes the cell membrane and simultaneously delivers proteins in a spatiotemporally precise and quantitative manner.

RESULTS AND DISCUSSION

FTag Screening and Optimization. The high electronegativity of organofluorines leads to mutual insolubility of many hydrophilic and lipophilic compounds, thus defining PFCs as fluorophilic.[28] This bioinert nature is critical to the persistence of PFC emulsions *in vivo*[41] and has been exploited to develop fluorinated coatings to inhibit surface biofouling.[42−44] These examples highlight the incompatibility of hydrophilic biologic materials and fluorous media. To overcome this physicochemical mismatch, we screened a small library of fluorochemical FTags to test their potential to complex with biomacromolecular proteins and mediate their efficient dispersion within PFCs, first using green fluorescent protein (GFP) as a model.

Screening experiments were performed using 12 FTags (Figure 2a and Table S1) rationally selected based on their potential to form hydrogen or ionic bonds with the solvent exposed protein surface. This ensures that candidate FTags noncovalently complex with and facilitate dispersion of proteins, while avoiding permanent chemical modification of the biologic. Each FTag was screened in excess with respect to GFP (13−1333:1 molar ratio), and the percentage of protein dispersed into perfluorohexane (PFH; an FDA-approved PFC[45]) was quantified *via* fluorescence spectroscopy (Figure 2b and Figure S1). It is worth noting that the intrinsic fluorescence of GFP is dependent of maintaining the protein's proper folded state.[46] Thus, this fluorescence-based screen identifies FTags that not only promote GFP solubility in PFH but also preserve the secondary and tertiary structure of the dispersed protein. Our results show that, as expected, GFP alone is insoluble in PFH (see entry Ø). However, FTag 6, the ionic perfluorononanoic acid (hereafter referred to as PFNA), showed a distinct capacity for fluorous masking that results in robust dispersion of GFP into PFH (Figure S2).

As shown in Figure 2c, increasing the molar ratio of PFNA/GFP results in a corresponding increase in protein dispersion efficiency, reaching a maximum of ~60% at ratios of 2667:1−13333:1. Interestingly, increasing the concentration of PFNA to ~60000:1 resulted in a complete loss of GFP solubilization (see highest ratio in Figure 2c) and formation of protein flocculates. This suggests there exists a critical threshold where increasing protein fluorination triggers self-association into large FTag−protein aggregates. These precipitates are subsequently removed during the centrifugation step of our dispersion protocol to ensure only soluble protein is assayed.

As will be demonstrated later, FTag-masked proteins can be efficiently loaded and spatiotemporally delivered from fluorous nanoemulsions under US. For these applications, the more volatile perfluoropentane (PFP) is preferred as its low boiling point (bp = 29 °C) should require less energy to vaporize[47]

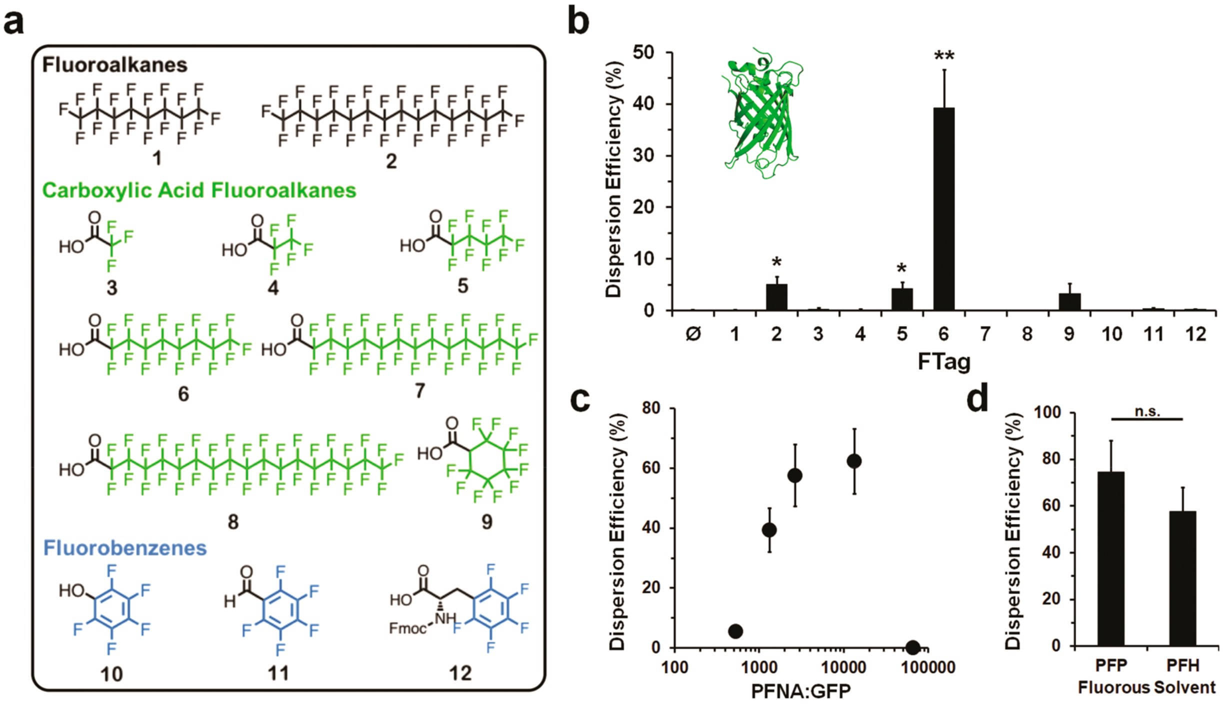

Figure 2. FTag-mediated protein dispersion into perfluorocarbons. (a) Structure of selected FTags screened in this work. (b) FTag screen to identify fluorous masking agents capable of dispersing GFP into the PFH solvent (Ø = no FTag). Results displayed as percent soluble protein (corrected for solvent effects) relative to initial loading for the 1333:1 FTag/protein molar ratio (additional screening ratios are reported in Figure S1). Statistical significance determined relative to control (Ø), with * indicating $p < 0.01$ and ** indicating $p < 0.001$. (c) Effect of PFNA (FTag 6)/GFP molar ratio on protein dispersion efficiency in PFH. (d) Efficiency of protein dispersion into PFP and PFH at the PFNA/GFP ratio of 2667:1 (n.s. = not statistically significant). All data shown as mean ± SEM for n = 9 replicates per condition.

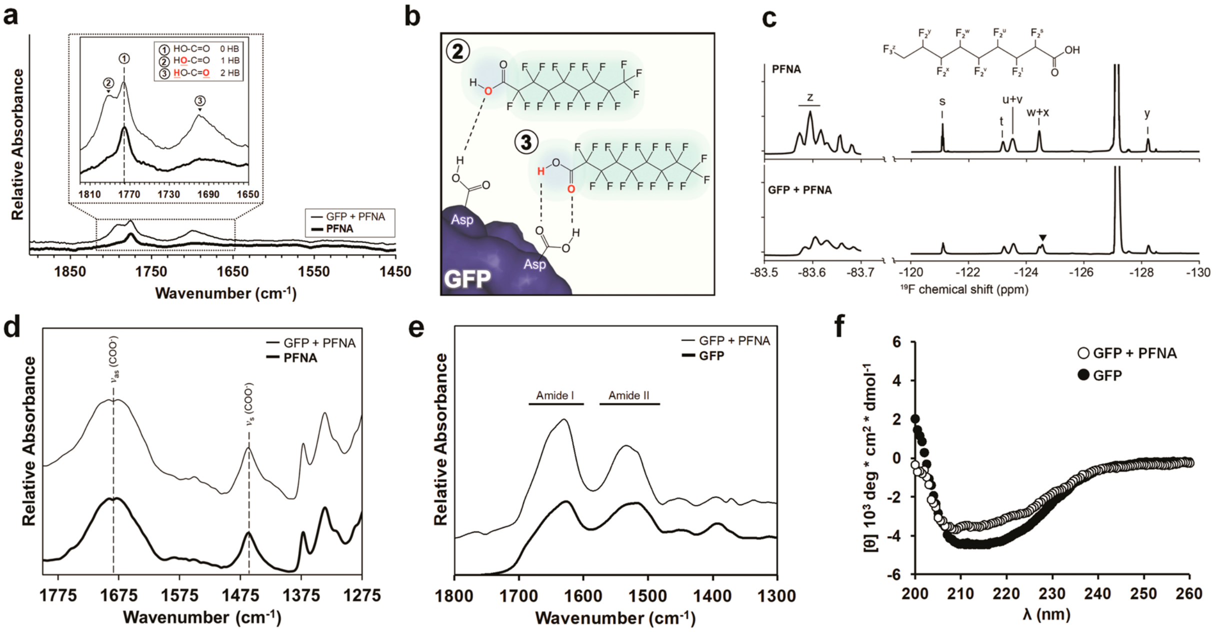

Figure 3. Biophysical characterization of FTag−protein complexes and vaporization-triggered unmasking. (a) Attenuated total reflectance Fourier transform infrared (ATR-FTIR) spectra of PFNA ± GFP (1333:1 molar ratio) in PFH. Inset: PFNA carboxy-specific spectral features in the mid-IR regime. Unbonded PFNA is defined by peak ①, whereas frequency shifts ② and ③ identify emerged peaks resulting from single and dihydrogen bonding interactions, respectively, between the FTag and GFP. (b) Schematic representation of PFNA complexed to solvent-exposed amino acids of GFP (aspartic acids shown as example residues). (c) ^{19}F NMR chemical shifts of PFNA ± GFP (2667:1 molar ratio) in PFH. Peak assignments (s−z) are defined in the inset chemical structure; ▼ denotes a shift observed following hydrogen-bond-mediated complexation of PFNA with GFP. (d,e) ATR-FTIR spectra of (d) PFNA or (e) GFP following decomplexation of the two components upon PFH vaporization (1333:1 molar ratio PFNA/GFP). Spectrum normalized to free GFP or PFNA alone, for panels (d) and (e), respectively, to remove contribution of the complementary component. (f) Circular dichroism spectra of GFP before (●) and after (○) complexation with PFNA and dispersion into PFH.

and therefore minimize protein damage relative to the PFH solvent (bp = 56 °C) employed in our FTag screens. Gratifyingly, PFNA shows no significant difference in GFP dispersion when comparing PFP and PFH solvents (Figure 2d).

Biophysical Interrogation of Protein Fluorous Masking. To probe the biochemical basis of FTag-mediated protein masking and to further investigate the role fluorine−fluorine interactions play in protein dispersion within PFCs, we conducted a series of biophysical analyses employing Fourier transform infrared (FTIR), ^{19}F nuclear magnetic resonance (^{19}F-NMR), and circular dichroism (CD) spectroscopies. First, FTIR experiments were performed to monitor changes in the chemical state of PFNA when complexed to the model protein GFP and dispersed into PFH. Results in Figure 3a (black line) demonstrate that PFNA, in the absence of protein, displays a single spectral feature in the functional group regime (4000−1450 cm^{-1}) at 1775 cm^{-1} (①), defining its carbonyl C═O stretch. This characteristic feature is expected to shift during intermolecular interactions and thus can be used to probe the chemical state of the FTag's carboxyl group during protein interactions. Indeed, introduction of GFP led to the emergence of two additional carbonyl-specific peaks at 1795 and 1701 cm^{-1} (Figure 3a; gray line; ② and ③). Peak ② represents a blue shift of the C═O stretching mode by +20 cm^{-1}, which aligns with the predicted frequency for one hydrogen bond at the hydroxyl oxygen (HO−C═O).[48] Peak ③ is red-shifted from −74 to 1701 cm^{-1}, matching the C═O stretching frequency for two hydrogen bonds (HO−C═O).[48] Taken together, this strongly suggests that association of PFNA with GFP is mediated *via* hydrogen bonding of the FTag carboxylic acid to the protein, presumably with the solvent-exposed amide backbone and/or polar side chains (Figure 3b). That said, our data does not rule out the possibility of electrostatic interactions between the PFNA carboxylate and protein basic residues, which may also contribute to the formation of FTag masks.

To further investigate this fluorous masking phenomenon as well as to quantify the number of FTags bound per protein, complementary ^{19}F NMR studies were performed. Chemical shifts and peak assignments for PFH and PFNA were defined from control spectra collected for each component (Figure 3c and Figure S3). Upon addition of GFP, broadening of PFNA peaks s, y, and z was observed as a result of protein interaction and chemical exchange, suggesting reversible binding. Furthermore, all PFNA peaks (s−z) experience an increase in shielding, as evidenced by their upfield shift (Figure S4). When taken together with our FTIR results (Figure 3a), this suggests that interaction of the PFNA carboxylic acid with the protein increases the net dipole moment toward the fluorines in the FTag tail. In turn, this increases the electron density and shielding of the $-CF_2$ and $-CF_3$ groups. One notable chemical shift was the emergence of an upfield signal from the fluorocarbon w + x peak (denoted as ▼ in Figure 3c). This spectral shift indicates that these $-CF_2$ groups experience particularly high shielding due to their close proximity to other fluorine atoms in neighboring PFNA FTags decorating the protein surface. Importantly, this spectral feature defines the protein-bound fraction of PFNA. Using Lorentzian−Gaussian peak fitting, we calculate that 65% of the PFNA available in solution is bound to GFP (Figure S5), which corresponds to 1731 molecules of PFNA complexed per dispersed protein.

So far, results of our screening and biophysical studies collectively demonstrate that a >1000 molar excess of PFNA is required to effectively mask GFP and mediate its dispersion into PFCs. Next, we investigated the potential for proteins to shed this fluorous coating during solvent vaporization. This is important for future delivery studies as US-mediated vaporization of the fluoroemulsion carrier may result in the release of FTag−protein complexes instead of the desired free biologic. This scenario would likely lead to aggregation of the fluorous-masked protein in the physiologic milieu. To model US-mediated vaporization in our biophysical experiments, the PFH solvent was evaporated from PFNA−GFP dispersions and the dried residue was subjected to FTIR analysis (Figure 3d,e). After vaporization, we observe that the C═O stretching frequency of PFNA is restored to the parent state, as demonstrated by an analogous spectrum of dry PFNA in the absence or presence of GFP (Figure 3d). No significant change in amide I or amide II bands for the protein was observed (Figure 3e). This collectively demonstrates that noncovalent interactions between the FTag and protein are broken during PFC vaporization. Further, CD spectroscopy performed on GFP recovered from PFH demonstrates that the protein's β-sheet-rich secondary structure remains intact when loaded into the fluorous solvent (Figure 3f). Hence, we have identified an FTag capable of masking proteins to mediate their dispersal within fluorous solvents, while readily unmasking the protein payload during delivery without compromising its native conformational state or function.

US-Controlled Cytosolic Protein Delivery. Through a series of *in vitro* and *in vivo* assays, we investigated the potential for fluorous nanoemulsions to be loaded with FTag−proteins to enable on-demand cytosolic delivery of the biologic payload under US. This was first optimized using GFP-loaded formulations before moving onto antibody cargoes. To facilitate the preparation of cell-targeted fluorous nanoemulsions, we used a *de novo* designed peptide emulsifier with the sequence $F_FF_FF_FF_F$GGGCCGGKGRGD-NH$_2$ (F_F = pentafluorophenylalanine).[49] In brief, this peptide contains a fluorinated N-terminus that enables its assembly at the fluorous nanodroplet interface. Disulfide cross-linking of intermolecular cysteines stabilizes the assembled emulsion shell and allows for multivalent display of KGRGD at the nanoemulsion surface.[49] This enables localization of the nanoparticle to cell membranes *via* binding of RGD with extracellular integrins, which we have previously shown enhances cellular delivery of encapsulated cargo over non-targeted controls.[49]

Importantly, peptide-stabilized PFP emulsions possess a vaporization temperature above the bulk boiling point of the fluorinated solvent (29 °C), resulting in particles that are stable at 37 °C.[49] This is a consequence of the peptide's surfactant-like properties, which allows for control over particle size and, consequently, interior droplet pressure. This is explained by the Laplace pressure equation: $P_{\text{in}} = \frac{2\sigma}{R_{\text{H}}} + P_{\text{atm}}$, where internal droplet pressure (P_{in}) is inversely related to the particle radius (R_{H}). Therefore, as the droplet size decreases, the interfacial pressure on the core is increased, and as a result, the vaporization temperature of the fluorous liquid interior increases. In our previous studies, we found that peptide emulsions <750 nm in diameter possess sufficient interfacial pressure to keep the fluorous PFP liquid in a stable, superheated state at temperatures >37 °C.[49]

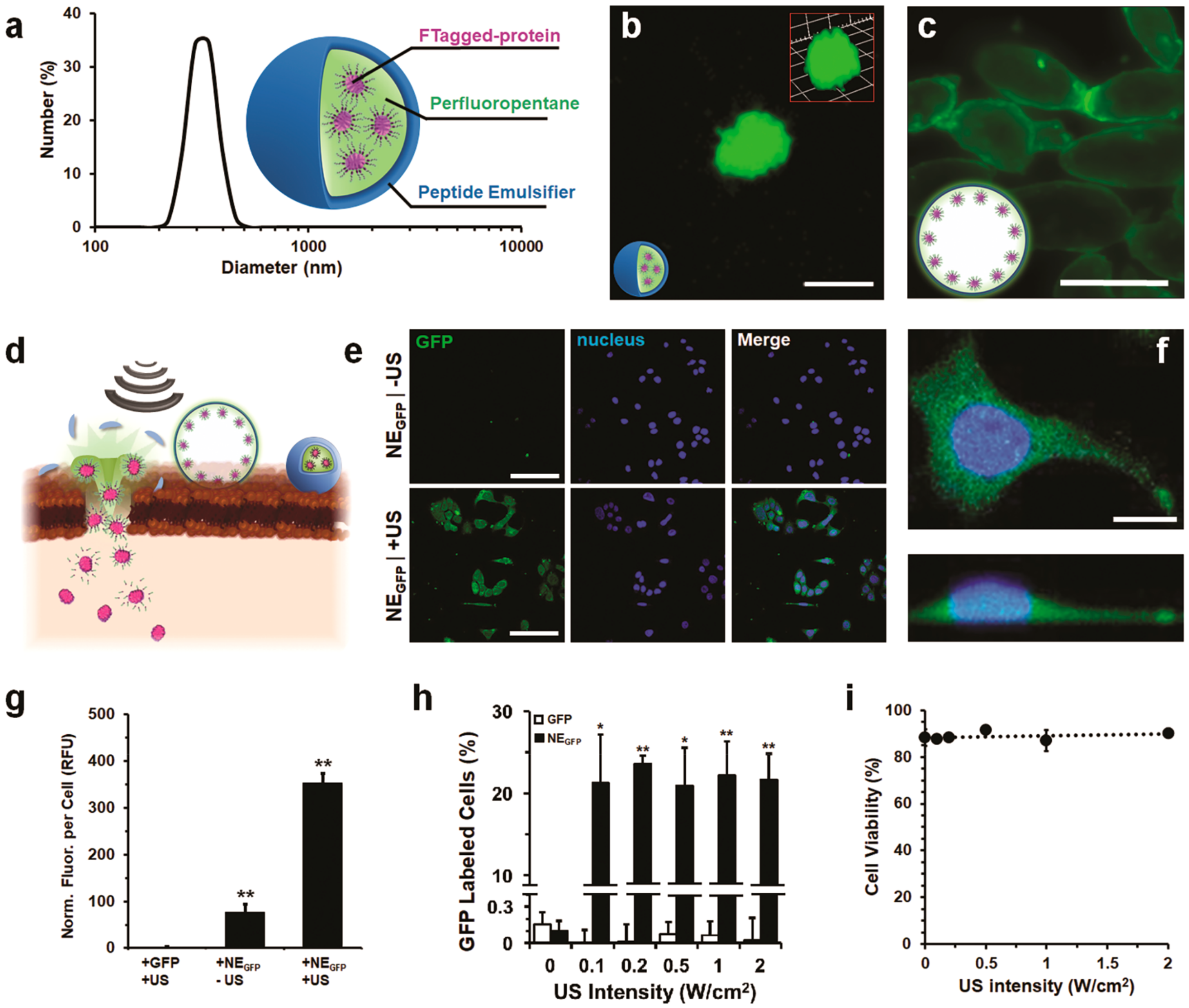

Figure 4. Formulation and US-triggered cytosolic GFP delivery from fluorous nanoemulsions. (a) Particle size and schematic representation of NE$_{\text{GFP}}$ particles. (b) Fluorescent micrograph of a single NE$_{\text{GFP}}$ particle (scale bar = 100 nm). Inset: z-stack image (scale bar = 300 × 300 nm). (c) Representative image of gaseous microbubbles formed following US-mediated vaporization of the NE$_{\text{GFP}}$ carrier (scale bar = 100 μm). (d) Proposed intracellular protein delivery mechanism from fluorous nanoemulsions. Binding of RGD-functionalized particles to the cell surface and US vaporization of the carrier leads to the formation of transient pores in the cell membrane and simultaneous delivery of the protein cargo (pink) directly into the cytoplasm. (e) Fluorescent micrographs of GFP delivery into A549 cells before (−US) and after (+US; 2 W/cm^2) acoustic activation of the NE$_{\text{GFP}}$ carrier (scale bar = 100 μm). (f) Magnification (top) and z-stack image (bottom) of a representative cell following intracellular delivery of GFP from NE$_{\text{GFP}}$ (scale bar = 10 μm). (g) Relative intracellular fluorescence (in relative fluorescence units) of A549 cells treated with NE$_{\text{GFP}}$ particles or free GFP as a control, +/− the US trigger. (h) Flow cytometry analysis of GFP positive cells following exposure to increasing US intensities in the presence of the free protein (open bars) or NE$_{\text{GFP}}$ particles (filled bars). Statistical significance relative to free GFP controls indicated by * = $p < 0.01$ and ** = $p < 0.001$. (i) Viability of A549 cells following NE$_{\text{GFP}}$ particle activation at clinically relevant intensities of US.

With this in mind, we prepared PFP-based peptide emulsions containing FTag−GFP, hereafter referred to as NE$_{\text{GFP}}$, with a mean particle size of ~300 nm (Figure 4a). Fluorescence spectroscopy studies revealed a GFP encapsulation efficiency of 71%, suggesting a fraction of the FTag−protein (~29%) may interact with the peptide emulsifier to produce nonfunctional aggregates. These off-pathway assemblies are subsequently removed during gravity-based particle purification. Fluorescence confocal microscopy demonstrated the productive assembly of protein-loaded nanoemulsions (Figure S6) and confirmed that the GFP cargo is dispersed uniformly within the fluorous liquid interior of the carrier (Figure 4b) and not simply adsorbed to its surface. US vaporization of NE$_{\text{GFP}}$ particles produced stable gaseous microbubbles containing intact fluorescent protein (Figure 4c), which partitioned to the gas−liquid interface during acoustic carrier activation.

With GFP-loaded nanoemulsions successfully prepared, we next optimized the ability of this platform to potentiate direct cytosolic transduction of protein cargo into cells under US. Here, vaporization and nonlinear expansion of the emulsion under US leads to violent collapse of the formed microbubble at the cell surface, a process referred to as inertial cavitation.[50−52] A high-velocity fluid jet formed during asymmetric bubble cavitation penetrates the cell membrane to form a transient pore[39,53] and, in our system, simultaneously delivers the protein payload directly into the cytoplasm (Figure 4d). To test this delivery mechanism, human A549 cells were incubated with NE$_{\text{GFP}}$ and subjected to varying conditions of US. Fluorescent confocal micrographs shown in Figure 4e

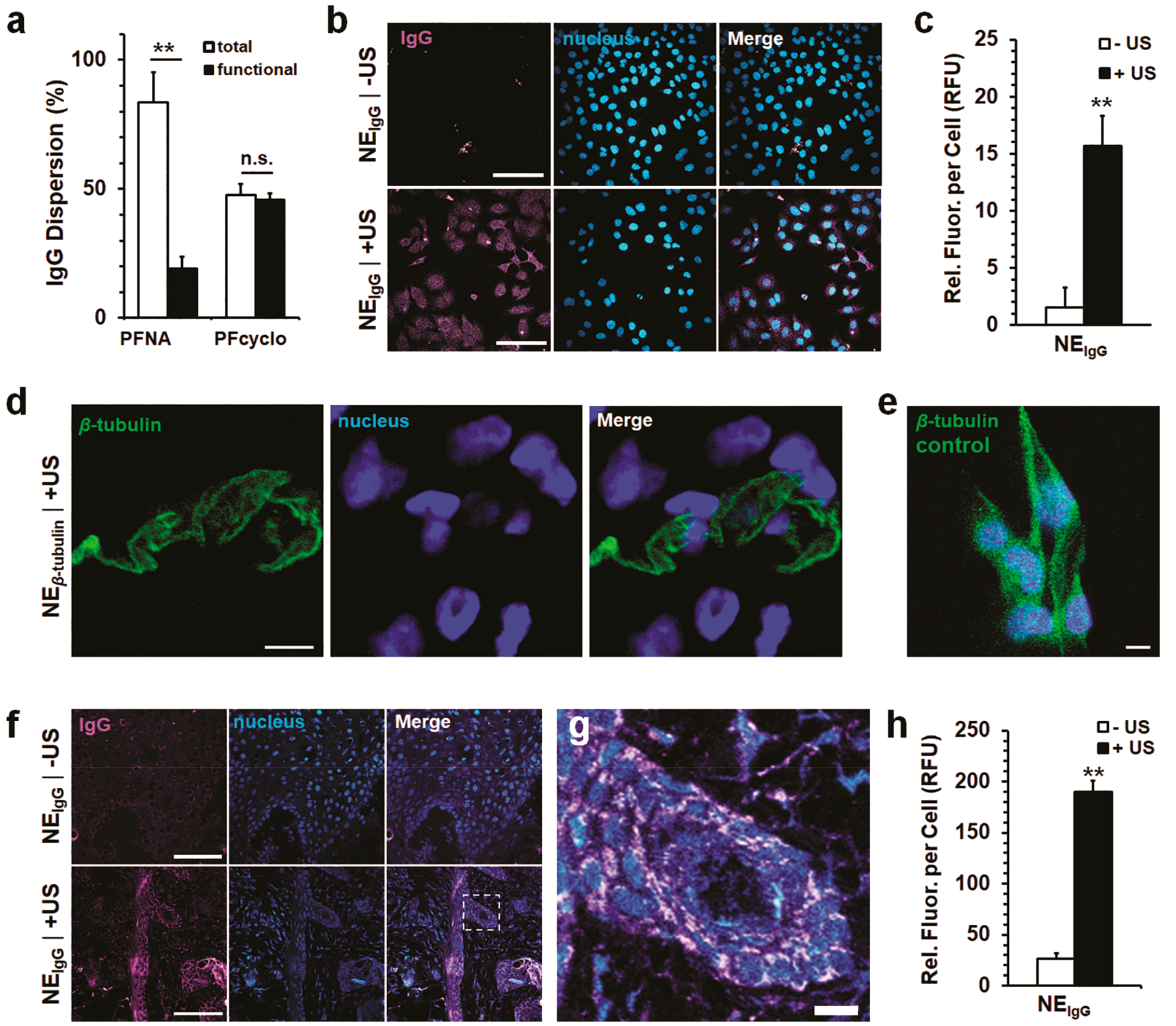

Figure 5. US-controlled intracellular IgG delivery *in vitro* and *in vivo*. (a) Comparison of functional *vs* total IgG dispersion between PFNA and PFcyclo. Data shown as mean ± SEM for $n = 9$ replicates per condition. (b) Fluorescent micrographs of *in vitro* IgG delivery into A549 cells before (−US) and after (+US; 1 W/cm^2) US activation of NE$_{IgG}$ particles (scale bar = 100 μm). (c) Relative intracellular fluorescence (in relative fluorescence units) of A549 cells treated with NE$_{IgG}$ particles +/− the US trigger. (d) Fluorescent micrographs of anti-β-tubulin antibody delivery into A549 cells after (+US; 1 W/cm^2) acoustic activation of NE$_{\beta\text{-tubulin}}$ particles (scale bars = 10 μm). (e) Control cells stained with the free β-tubulin antibody (scale bars = 10 μm). (f) Immunofluorescent micrographs of squamous epidermal tumor sections 5 days after administration of NE$_{IgG}$ without (−US) and with (+US; 2 W/cm^2) application of the US trigger (scale bar = 1 mm). (g) ROI magnification (white dashed square in panel f), demonstrating intracellular delivery of IgG following US activation of NE$_{IgG}$ particles (scale bar = 10 μm). To maximize the fluorescent signal during the *in vivo* studies, PFNA was selected as the biofluorinating agent to prepare NE$_{IgG}$ particles. Results for analogous *in vivo* studies using PFcyclo formulations can be found in Figure S14. (h) Relative intracellular fluorescence (in relative fluorescence units) of squamous tumor cells isolated from InvtTA × tetORas mice following treatment with NE$_{IgG}$ particles +/− the US trigger. Data in panels (c) and (h) are shown as mean ± SEM for $n = 100$ cells per condition. Statistical significance of results relative to appropriate controls shown with ** indicating $p < 0.001$ (n.s. = not statistically significant).

demonstrate that, in the absence of the acoustic trigger, NE$_{GFP}$ particles remain intact and do not spontaneously deliver the GFP payload. Conversely, rapid transduction of GFP into cells is observed when NE$_{GFP}$ particles are activated with the US trigger. Careful inspection of treated cells shows that delivered GFP is disseminated throughout the intracellular volume (Figure 4f), suggesting direct cytoplasmic localization. Semi-quantitative analysis of intracellular fluorescence, shown in Figure 4g, demonstrates that >150 times more GFP is delivered into cells following US activation of NE$_{GFP}$ compared to controls insonated in the presence of the free protein (see Figure S7 for fluorescent micrographs of controls). Notably, in the absence of US, we observed a small degree of nonspecific particle internalization into cells (see Figure 4g; +NE$_{GFP}$, −US). Given the size of these nanoemulsions (~300 nm), and their ability to bind to cell-surface integrins, this nonspecific uptake is most likely due to a combination of receptor-mediated endocytosis and macropinocytosis.[54,55]

Next, we investigated how US intensity impacts the intracellular transduction efficiency of delivered GFP. Results in Figure 4h show that as low as 0.1 W/cm^2 of the acoustic trigger is sufficient for robust delivery from NE$_{GFP}$ particles, with little apparent variation in efficacy as the US intensity is increased. As before, NE$_{GFP}$ particles remain inactive in the

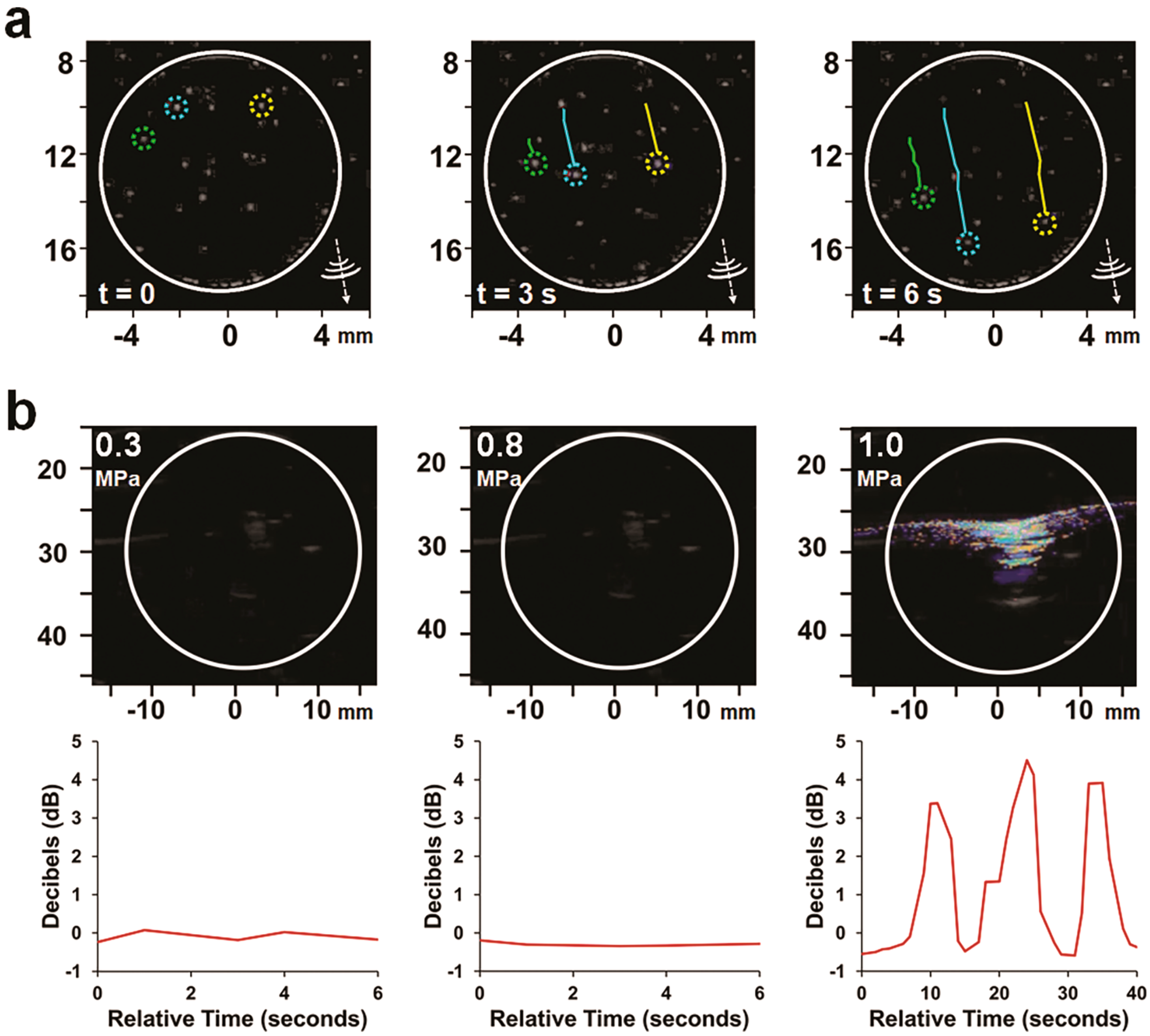

Figure 6. Real-time US imaging and guidance of protein-loaded nanoemulsions. (a) High-resolution B-mode US (18.5 MHz) of NE_{GFP} encapsulated within an agarose phantom (defined by the white circle). Images shown at t = 0−6 s; three representative particles are tracked (green, blue, and yellow). Nanoemulsions are guided in the gels along the axis of the applied acoustic pulse (direction of US shown in bottom right). (b) Top: Doppler US imaging (5 MHz) of NE_{GFP} vaporization and inertial cavitation of microbubbles as the acoustic pressure is increased. No signal is observed at pressures below the particle's inertial threshold (~0.9 MPa). Cavitation above this pressure threshold is observed as transient Doppler twinkling (1.0 MPa image shown as stacked twinkling events collected over a 40 s interval; see Movie S2). Bottom: Quantitation of Doppler magnitude due to bubble collapse as a function of time. Transient collapse events were recorded at pressures above the empirically determined cavitation threshold of the particles.

absence of the US trigger (0 W/cm^2, intracellular fluorescence is near zero), and the free protein is unable to enter cells even when mechanically driven by US. Finally, cells remain viable and proliferative when insonated in the presence of NE_{GFP} (Figure 4i), and the delivered GFP payload is unharmed and bioactive (Figure S8). Taken together, these results demonstrate that US-responsive fluorous nanoemulsions can be acoustically activated to afford temporal and on-demand intracellular protein delivery without compromising cellular viability or integrity of the biologic payload.

US-Guided Antibody Transduction. With acoustic protein delivery validated for GFP-loaded fluorous nanoemulsions, we next tested the capability of this platform to enable controlled and cytoplasmic transduction of high molecular weight antibodies in *in vitro* cultures and in a transgenic *in vivo* model of cutaneous squamous cancer. For these studies, purified rabbit IgG (~150 kDa) was used and subjected to our protein dispersion screening workflow to select an appropriate FTag (Figure S9). Two candidate FTags, **6** (PFNA) and **9** (perfluorocyclohexanecarboxylic acid, PFcyclo), demonstrated robust PFC solubilization of IgG with an optimized dispersion efficiency of 84 and 52%, respectively (Figure S10). As with our previous experiments, PFNA demonstrated the greatest propensity for IgG masking and dispersion into PFH. However, complementary CD spectroscopy (Figure S11) and F_c functional titer assays (Figure 5a) indicate that much of the fluorinated antibody is denatured and inactivated during PFNA-mediated dispersion. We therefore turned to our second FTag candidate, PFcyclo, which also showed efficient loading of IgG into the fluorous solvent (Figures S9 and S10) while maintaining the proteins' native structure and function (Figure 5a and Figure S11). This differential in masking performance may be related to the disparate acidity of the two carboxylic-acid-containing FTags. PFNA is a significantly stronger acid ($pK_a = -0.6$) compared to PFcyclo ($pK_a = 1.7$), suggesting that FTag pK_a, and thus hydrogen bonding propensity, may require optimization for each protein cargo to favorably balance dispersion efficiency and protein structural integrity.

Selecting PFcyclo for IgG dispersion, NE_{IgG} nanoemulsions were prepared using the RGD-containing peptide emulsifier and found to possess an average particle size of 580 nm (Figure S12). Titer assays performed on US-disrupted particles indicate an IgG encapsulation efficiency of 80%. Fluorescent confocal microscopy studies confirm that NE_{IgG} particles enable on-demand and temporally controlled delivery of encapsulated antibodies into cells only when activated *via* US (Figure 5b), resulting in >10 times the amount of IgG transduced into the cytoplasm when compared to control particles left unexposed to US (Figure 5c). Quantification of intracellular IgG concentration *via* F_c titer assays indicated approximately 1.25 μM of cytosolic IgG was delivered per cell. Gratifyingly, this concentration is orders of magnitude above the binding affinity of many antibodies, which typically possess K_d values that are in the low nanomolar range.

Although these *in vitro* results are encouraging, we next sought to validate the utility of this platform to deliver a bioactive antibody with a defined cytosolic target. Utilizing PFcyclo as the FTag masking agent, we prepared nanoemulsions containing a fluorescently labeled anti-β-tubulin antibody ($NE_{\beta\text{-tubulin}}$) and performed confocal microscopy experiments to assess its functional activity after US-mediated delivery into A549 cells. Fluorescent confocal micrographs shown in Figure 5d,e and Figure S13 confirm that bioactive anti-β-tubulin antibodies can be delivered to the cytoplasm of cells following $NE_{\beta\text{-tubulin}}$ particle activation. More importantly, this validates that FTag transient masking of antibodies does not compromise their bioactivity, as confirmed by the ability of delivered anti-β-tubulin to bind cytoskeletal tubulin filaments.

To demonstrate proof of principle for *in vivo* delivery, we employed a bitransgenic mouse model in which human $HRas^{G12V}$ is expressed in the skin under the control of a doxycycline regulated tet transactivator, Inv-tTA. Reduction of the suppressive doxycycline dose causes the formation of cutaneous squamous papillomas.[56] Rabbit serum IgG-loaded nanoemulsions (NE_{IgG}) were administered retro-orbitally to tumor-bearing mice and allowed to circulate for up to 5 days with multiple exposure of epidermal lesions to US (2 W/cm^2) at specific time points. Adjacent tumors in the same mice were left uninsonated as a control. Fluorescent confocal micrographs of cyrosectioned tissues confirm IgG is successfully delivered to the area of tissue exposed to the exogenous US pulse, whereas negligible delivery was observed in the uninsonated tumor (Figure 5f and Figure S14). Careful inspection of tissue sections suggests the antibody payload is indeed delivered to the cytoplasm of insonated tumor cells (Figure 5g) rather than being nonspecifically ejected into the interstitial space. Semiquantitative analysis of squamous tumor cells isolated from treated InvtTA × $tetOHRas^{G12V}$ mice reveals that >7 times the amount of IgG is delivered into cells following NE_{IgG} vaporization compared to unactivated controls (Figure 5h). Collectively, our data demonstrates that US-responsive fluorous nanoemulsions can be activated in tissues to successfully afford intracellular delivery of antibodies with temporal control.

Real-Time Carrier Guidance and Monitoring. In addition to their antibody delivery potential, fluorous nanoemulsions can act as an acoustic contrast agent to allow their imaging-based guidance in tissues using clinically relevant diagnostic US modalities. To demonstrate this for our protein-loaded formulations, B-mode US (18.5 MHz) was performed on nanoemulsions formulated with the model GFP payload and enclosed within a tissue-mimetic agarose phantom. B-mode imaging encodes the scattered acoustic wave into grayscale pixels, with brighter pixels indicative of a more highly scattering surface. As shown in Figure 6a, NE_{GFP} particles are hyperechogenic and can be clearly resolved under B-mode. Further, the particles can be guided in the tissue analogues along the direction of the applied acoustic pressure wave (see particle tracking in Figure 6a and Movie S1). In these experiments, the detected NE_{GFP} particles are most likely vaporized nanoemulsions that have phase-shifted into stably oscillating microbubbles. This assertion is based on the direct proportionality of acoustic scattering and particle size.[57,58] Hence, liquid nanoemulsions are significantly less echogenic relative to their gaseous microbubble counterparts. Yet, it is clear that not all of the NE_{GFP} have vaporized under these conditions as the density of detected particles is well below the loaded concentration. This suggests that a small population of particles undergo an early liquid−gas phase transition at the low diagnostic intensities employed for these imaging experiments. Opportunely, these bubbles serve as hyperechogenic "beacons" that can be used for auxiliary guidance of the remaining bulk population of stable nanoemulsions, which are otherwise difficult to resolve using clinically relevant B-mode modalities. Given that the acoustic intensity required to vaporize droplets is inversely related to particle size, it is presumed that the largest emulsions within the population of NE_{GFP} particle sizes (300−500 nm; see Figure 4a) are responsible for the formation of these microbubble beacons.

In separate experiments, color Doppler US (5 MHz) was employed to measure the pressure threshold at which NE_{GFP} particles undergo inertial cavitation and to directly observe the collapse of vaporized microbubbles in real-time. Here, acoustic scattering from oscillating bubbles is interpreted by the US transducer as isotropic bubble movement, thus displaying what is known as a "twinkling artifact". Results shown in Figure 6b confirm that at low acoustic pressures (0.3−0.8 MPa), below the threshold for inertial bubble cavitation, no Doppler signals are observed as the NE_{GFP} particles stably oscillate. However, as the acoustic pressure is increased to ≥0.88 MPa transient twinkling events occur as the NE_{GFP} bubbles collapse (see 1.0 MPa panel in Figure 6b). These pulses occur rapidly and at a duration of approximately 1 event per second (Movie S2). Quantitation of the Doppler response by converting the imaging signal into decibels (dB) allows for the isolation of discrete bubble cavitation events over time (Figure 6b, lower panels). These results highlight the potential for Doppler ultrasonography to be used to monitor the vaporization and collapse of individual nanoemulsions. This may lead to the possibility of directly quantifying the amount of delivered cargo from the ruptured carrier in real-time using imaging techniques already employed in the clinic.

CONCLUSION

Loading proteins into nanoparticle carriers and efficiently releasing them to cells remains a significant challenge. For fluorous emulsions, the predominant strategy, particularly for biologics, remains chemical or physical attachment of the payload to the particle surface *via* intermolecular interactions. Once localized to the cell surface, US vaporization and bubble collapse expels the payload to enable its passive diffusion across the acoustically cavitated membrane. However, these membrane openings rapidly reseal after poration, achieving complete closure in ∼4 μs.[59,60] Simple Stokes−Einstein diffusion estimates reveal that, even under ideal conditions, only a fraction of delivered cargo can diffuse into cells before pore closure. Thus, diffusion alone is not sufficient to achieve effective protein delivery from fluorous emulsions.

This conventional paradigm of surface-mediated loading and delivery has been, until now, necessitated by the inability to load hydrophilic small molecules and biologics into the fluorous emulsion core. We present a fluorous encapsulation approach that is enabled through the discovery of a family of FTag fluoro-amphiphiles capable of transiently masking hydrophilic proteins without altering their structural and functional integrity. This general methodology can be employed to transiently fluorinate a range of protein classes, including enzymes, cytokines, and growth factors. More importantly, the transient nature of this technique allows us to effectively "turn on" the bioactive function of intracellularly delivered protein cargoes *via* US-controlled unmasking. As a result, our work provides a different perspective to the emerging utility of fluoro-amphiphiles, particularly fluoropolymers,[61,62] for direct cytosolic transduction of bioactive proteins.

In this work, we exploit this transient fluorous masking strategy to prepare antibody-loaded emulsions and demonstrate that clinical US imaging modalities can be used to guide and trigger the localized nanoinjection of the immunoglobulin payload across the cell membrane and into the cytoplasm. Thus, this delivery platform will not only advance strategies in precision medicine but also may nucleate the design of US-controlled nanoscale tools that impact the fields of stem cell and tissue engineering, drug discovery, gene editing, and developmental biology, all while leveraging the portable and noninvasive nature of diagnostic US.

EXPERIMENTAL METHODS

Materials. All FTags were purchased from suppliers noted in Table S1. Perfluorohexane (PFH) and perfluoropentane (PFP) were purchased from Oakwood Chemicals and Strem Chemicals, respectively. All Fmoc-protected amino acids, rink amide ProTide (LL), and Oxyma Pure were purchased from CEM. Trifluoroacetic acid (TFA) and LC-MS grade acetonitrile were purchased from Fisher Chemical. *N*,*N*-Diisoproylcarbodiimide (DIC) and thiazolyl blue tetrazolium bromide (MTT) were purchased from Chem Impex. Anisole was purchased from TCI. Thioanisole and dimethyl sulfoxide (DMSO) were purchased from Alfa Aesar. 1,2-Ethanedithiol and diethyl ether were purchased from Acros Organics. Slide-A-Lyzer dialysis cassettes (MWCO 3500 Da) were purchased from Thermo Scientific. Phosphate buffered saline (PBS) 1× without calcium and magnesium, fetal bovine serum (FBS), L-glutamine (L-Gln), and 0.25% trypsin EDTA were purchased from Corning. Gentamycin was purchased from VWR. RPMI-1640 without L-glutamine was purchased from Lonza. Hoechst 33342 and UltraPure agarose were purchased from Invitrogen. Paraformaldehyde (4%) in PBS was purchased from Chem Cruz. The green fluorescent protein (GFP, 36 kDa) and A549 lung carcinoma cell line were kindly donated by the laboratory of Dr. Joel P. Schneider (Chemical Biology Laboratory, NCI). Purified IgG from rabbit serum and anti-rabbit IgG-FITC antibody produced in goat were purchased from Sigma-Aldrich. Pierce Coomassie Plus (Bradford) assay reagent, an Easy-Titer rabbit IgG assay kit, and ProLong Diamond antifade mountant with DAPI were purchased from ThermoFisher Scientific.

Protein Dispersion. Twelve FTags were screened for dispersal of proteins into PFH. All FTags were dissolved at 0.01, 0.1, and 1 mM. FTag in PFH (200 μL) was added to dried GFP or IgG in Eppendorf tubes to a final protein concentration of 0.75 or 1 μM, respectively. Each tube was parafilmed, vortexed, and rotated overnight at 4 °C to mix. Samples were centrifuged for 5 min at 1610*g* to pellet insolubilized protein. For GFP, the sample supernatant (100 μL) was aliquoted into black bottom 96-well plates and incubated at 37 °C overnight to evaporate PFH. Dried residues were resuspended in 100 μL of PBS, and fluorescence emission was read at 510 nm (λ_{ex} = 470 nm) using a fluorescent plate reader (Biotek Cytation 3). GFP in PBS and blank PFH were used as positive and negative controls, respectively. For macroscopic images of GFP dispersion, samples of free protein (0.75 μM GFP in PFH) or FTag masked GFP (1 mM PFNA and 0.75 μM GFP in PFH) were transferred into Eppendorf tubes and photographed. For quantification of rabbit IgG dispersion, the sample supernatant (100 μL) was aliquoted into clear 96-well plates and incubated at 37 °C overnight to evaporate PFH. Dried residues were resuspended in 100 μL of PBS with equal parts Coomassie blue reagent for Bradford Assay. Samples were shaken at 25 °C for 10 min and absorbance read at 595 nm. IgG in PBS and PFH was used as a positive and negative control, respectively.

Molar ratio screening was performed following the protocol described above. Briefly, GFP was dispersed in PFH with perfluorononanoic acid (PFNA) at 0.4−100 mM (533:1−66667:1 PFNA/GFP molar ratio). For perfluorocarbon solvent comparison, GFP was dispersed in either PFH or PFP using 2 mM PFNA (2667:1 PFNA/GFP molar ratio). For the IgG molar ratio screening, IgG was dispersed in PFH with PFNA or perfluorocyclohexanecarboxylic acid (PFcyclo) at 0.01−10 mM (100:1−10000:1 FTag/IgG molar ratio). For functional IgG screening, IgG was dispersed in PFH with either 1 mM PFNA or PFcyclo (1000:1 FTag/IgG molar ratio). An Easy-Titer rabbit IgG assay kit was used to detect the amount of functional protein recovered based on the F_c binding region of IgG, and dispersion efficiency calculations were based on the IgG control at absorbance 340 nm. For protein dispersion screening analysis, the Grubb's test was performed for outlier removal before dispersion efficiency calculations. Dispersion efficiency (%) was background normalized and calculated in reference to positive controls.

Attenuated Total Reflection Fourier Transform Infrared Analysis. Attenuated total reflection (ATR)-FTIR measurements were performed using a Bruker Vertex V70 instrument equipped with a liquid-nitrogen-cooled wide band mercury cadmium telluride detector. Spectra were collected using a Diamond ATR crystal at a fixed incident angle of 45° on a Harrick MVP Pro ATR accessory. A total of 500 scans at 4 cm^{-1} resolution were averaged per spectrum with OPUS software used for data analysis. Liquid FTIR experiments were performed by dispersing GFP into PFH using PFNA (1333:1 PFNA/GFP ratio). This was achieved by adding 50 mM PFNA in PFH to GFP to reach a final target protein concentration of 37.5 μM. To prevent evaporation, a 1 cm Viton ring was placed around the crystal where the sample was then aliquoted and quickly covered by glass and manual pressure. For dry sample preparation, a 2667:1 molar ratio of PFNA and GFP was used to disperse the protein into PFH. After overnight mixing, the samples were centrifuged (5 min, 1610*g*) and the supernatant was aliquoted into a separate Eppendorf tube. Samples were then dried in a 37 °C incubator, and residues were manually transferred to the FTIR crystal for analysis. Three replicates were performed for each condition with representative spectra reported.

^{19}F NMR Studies. For ^{19}F NMR experiments, the FTag−protein complex interaction was studied at a 2667:1 PFNA/GFP molar ratio. Following sample mixing as defined above in the protein dispersion method, samples were aliquoted into Wilmad-LabGlass thin wall precision tubes with Norell coaxial inserts containing D_2O as a lock signal. NMR spectra were collected on a Bruker AVIII-HD-500 using a 30° flip angle (zg30 in the Bruker library) 1D pulse program. NMR measurements were performed at 298 K. Each NMR experiment consisted of 16 scans with an origin set at 20.72 ppm and a sweep width of 241.4655 ppm. Data were analyzed with Mnova software. Replicates (n = 3) were performed for each condition with representative spectra reported.

Circular Dichroism. Circular dichroism (CD) spectroscopy was performed on GFP (7.5 μM) or IgG (10 μM) recovered following dispersion into PFH or directly dissolved into buffer as a positive control. All samples were dissolved in CD-compatible buffer (50 mM BTP, 150 mM NaF, pH 7.4). For PFH-dispersed samples, GFP was dissolved at 1333:1 PFNA/GFP ratio and IgG at 1000:1 PFNA/IgG or PFcyclo/IgG. The postcentrifugation supernatant was aliquoted into a separate Eppendorf tube and dried at 37 °C to remove the PFH solvent before resuspension in CD buffer. Sample measurements were taken using a Jasco J-1500 circular dichroism spectrometer. Replicates (n = 3) were performed for each condition with representative spectra reported.

Peptide Synthesis and Purification. Using a CEM Liberty Blue microwave peptide synthesizer, peptides were synthesized *via* solid-phase Fmoc-based peptide chemistry with DIC activation on low-loading rink-amide ProTide resin. Peptide was prepared with an amidated C-terminus. Peptide was cleaved from resin, and side chains were deprotected with a cleavage cocktail (90:5:3:2, TFA/thioanisole/1,2-ethanedithiol/anisole) for 3 h while being stirred under argon. Crude peptide was precipitated by addition of cold diethyl ether, and the product was dried *via* lyophilization. Crude was purified *via* reverse-phase HPLC employing a Phenomenex semi-prep Luna C18 column and a gradient of 0−20% standard B over 10 min, followed by 20−100% standard B over 80 min. The collected product was then lyophilized to obtain pure peptide. Preparative HPLC solvents were composed of standard A (0.1% TFA in water) and standard B (0.1% TFA in 9:1 acetonitrile/water). The pure peptide was characterized by HPLC-MS (Shimadzu, LC-MS 2020; see Figure S15) equipped with a Phenomenex C18 analytical column (5 μm bead, 200 × 4.6 mm) using a gradient of 1% standard B per minute for 100 min. HPLC-MS solvents were composed of standard A (0.1% formic acid in water) and standard B (0.1% formic acid in 9:1 acetonitrile/water).

Nanoemulsion Synthesis and Characterization. To synthesize protein-loaded fluorous nanoemulsions (NE), GFP was dispersed into PFP using the PFNA FTag (2667:1 PFNA/GFP ratio), and IgG and anti-β-tubulin were dispersed into PFP using PFcyclo (1000:1 PFcyclo/Ab ratio), as described above in protein dispersion methods. FTag−protein in PFP (200 μL) was aliquoted into a separate tube containing $F_FF_FF_F$GGGCCGGKGRGD-NH_2 (final peptide concentration 0.65 μM). Samples were thoroughly mixed *via* extensive vortexing. To initiate peptide assembly and emulsification, the mixture was slowly added to chilled DI water (3 mL, stirred at 1200 rpm) in a 10 mL round-bottom flask kept on ice. In a typical experiment, 150 μL of the PFP solution containing peptide/protein/FTag was added dropwise into the stirred water. The emulsion was stirred for 1 h before being transferred to a Slide-A-Lyzer dialysis cassette (MWCO 3500 Da) for purification. Samples were dialyzed overnight against pure water containing 2.5% DMSO to allow for disulfide cross-linking of the peptide corona to stabilize the emulsions, as previously reported.[49] Prior to collection of NE particles, the samples were dialyzed against pure water for 1 h to remove DMSO.

NE_{GFP} and NE_{IgG} particle size was measured *via* dynamic light scattering using a Malvern Zetasizer Nano ZS. For these experiments, NE_{GFP}, NE_{IgG}, or $NE_{\beta\text{-tubulin}}$ were diluted 1:10 in TBS buffer (25 mM Tris, 150 mM NaCl, pH 7.4) and transferred to a polystyrene cuvette for analysis. NE_{GFP} confocal fluorescence microscopy was performed at a 1:10 dilution of NE_{GFP} in PBS added onto a glass slide with a coverslip. Samples were mounted onto a Zeiss LSM 800 confocal microscope with Airyscan and 63×/1.4 oil objective lens using 488 nm single photon laser for GFP signal detection. To image vaporized NE_{GFP} particles, epifluorescent microscopy was performed (Biotek Cytation 3, GFP filter cube λ_{ex} = 475 nm, λ_{em} = 525 nm) on a particle suspension activated using a sonicating water bath. For these experiments, particles which could be stably vaporized without collapse were needed. We therefore employed NE_{GFP} emulsions formulated at final peptide concentration of 0.9 μM to stabilize the emulsion shell and allow for production of intact microbubbles following sonication.

GFP Post-ultrasound Fluorescence. Using a 12-well plate, 1 mL of GFP (1 μM) in PBS was treated with ultrasound using a Nepagene Sonitron GTS with a plane wave transducer (0.1−2.0 W/cm^2, 20% duty cycle, 90 s) for three replicates per intensity. Blank buffer and a solution of 1 μM GFP that was not exposed to ultrasound served as negative and positive controls, respectively. Fluorescence emission was scanned over 500−560 nm (λ_{ex} = 470 nm) using a fluorescent plate reader (Biotek Cytation 3) and normalized to the positive control to evaluate the change in protein fluorescence.

***In Vitro* Intracellular Protein Delivery from Fluorous Nanoemulsions.** For GFP and IgG confocal microscopy studies, A549 cells were seeded at either 5.4 × 10^3 cells/well or 10 × 10^3 cells/well, respectively, in a 12-well plate containing a sterilized coverslip in each well and adhered overnight at 37 °C. Particle treatment solutions were diluted in serum-free RPMI-1640 media at various volume ratios (NE_{GFP} = 1:5, NE_{IgG} = 1:10, $NE_{\beta\text{-tubulin}}$ = 1:5) and added to the cells. A similar concentration of free protein, GFP (2.25 μg/mL), IgG (56.13 μg/mL), and anti-β-tubulin (10 μg/mL) in serum-free media was employed as a control. Samples were then incubated for 4 h to allow for binding of the RGD-targeted particles to the surface of cells before addition of 1 mL of serum-free media. Ultrasound activation of the particles was performed using a Nepagene Sonitron GTS with a plane wave transducer (1 MHz, 20 mm diameter). The transducer was held with a ring stand and lowered to ∼0.25 cm from the bottom of the plate during insonation. Ultrasound was applied at 0.1−2.0 W/cm^2 and 20% duty cycle for 90 s. After that, cells were allowed to recover for 30 min at 37 °C and then gently washed with 1 mL of serum-free media. Cells were fixed with 1 mL of 4% paraformaldehyde in PBS for 10 min at room temperature. For NE_{GFP}, fixative was aspirated, and cell nuclei were stained by incubating cells for 15 min with 2 μg/mL of Hoechst 33342. Cells were then washed with PBS before recovering the coverslip and mounting it onto a glass slide. For NE_{IgG}, fixative was aspirated and then cells were permeabilized (0.1% Trition-X100 in PBS) for 15 min at room temperature. After aspiration of permeabilizing solution, the cells were blocked (0.1% Tween-20, 1% BSA in PBS) for 24 h at 4 °C and treated with goat anti-rabbit IgG-FITC antibody (1:2000) for 1 h at room temperature. NE_{IgG} and $NE_{\beta\text{-tubulin}}$ samples were washed with PBS before mounting the coverslip with ProLong Diamond antifade mountant with DAPI onto a glass slide. Samples were imaged on an Olympus Fluoview 1000 confocal microscope with a PlanApo 40×/1.4 oil objective lens using 405 and 488 nm single photon lasers for Hoechst/DAPI and GFP/FITC/AlexaFluor-488 signals, respectively. Relative intracellular fluorescence was semiquantitatively analyzed *via* ImageJ. Calculated average fluorescence per cell normalized by untreated cell control is shown as mean ± SEM for n = 100 cells per condition.

For quantification of IgG intracellular delivery using NE_{IgG} (1:5) and US (1.0 W/cm^2), cytoplasmic proteins were extracted from cells using M-PER mammalian protein extraction reagent for 5 min. Cell lysate was collected and centrifuged at 14000g for 10 min. An Easy-Titer rabbit IgG assay kit was used to detect the amount of functional protein delivered based on the F_c binding region of IgG. The amount of IgG delivered was normalized to the untreated and −US control at absorbance 340 nm. IgG concentration per cell cytoplasm was calculated based on 50000 cells per well, and a total A549 cytoplasmic volume of 875 μm^3.

For flow cytometry studies, 2.5 × 10^5 A549 cells/well were added to 12-well plates and immediately mixed with NE_{GFP} particles in serum-free RPMI-1640 media to achieve a final volume of 1 mL (1:4 dilution of the stock particle solution into media). The mixture was then incubated in the dark for 4 h with gentle shaking (40 rpm) to prevent cell adhesion to the plates. As a control, A549 cell suspensions were co-incubated with free GFP at an equivalent protein concentration as was loaded into NE_{GFP} particles (2.25 μg/mL). Next, an additional 1 mL of serum-free media was added to each well before insonation using the Nepagene Sonitron GTS system.

https://dx.doi.org/10.1021/acsnano.9b08745

Ultrasound was applied for 90 s at 20% duty cycle and 0.1−2.0 W/cm^2, followed by incubation of the plates in the dark for 30 min while being shaken before being transferred to sterile Eppendorf tubes and centrifuged for 5 min at 2000 rpm. The supernatant was aspirated, and 500 μL of PBS was added. The cells were placed on ice and vortexed before analysis using a BD LSR Fortessa flow cytometer (488 nm excitation laser). Gating was based off of untreated A549, and FlowJo software was used for analyze cytometry results. Each condition was replicated at an $n \geq 3$.

Toxicity of Ultrasound Activated NE$_{GFP}$ Particles. A549 cells were seeded at 1 × 10^5 cells/well on a 12-well plate using RPMI-1640 media supplemented with FBS (10% v/v), L-Gln (2 mM), and gentamycin (0.05 mg/mL). Cells were treated with a 1:4 dilution of NE$_{GFP}$ particles in serum-free media and incubated for 4 h at 37 °C before insonation (0.1−2.0 W/cm^2, 20% duty cycle, 90 s). Negative control cells were treated with media, and positive control cells were treated with 20% DMSO. Insonated cells recovered for 30 min before the aspiration of media and addition of 1 mL of MTT solution (0.5 mg/mL). After a 2 h incubation, supernatant was aspirated and formazan product was solubilized by addition of 1 mL of DMSO. Absorbance was read at 540 nm using a BioTek Cytation 3 imaging reader. Percent viability was calculated with the following equation: $(\text{absorbance}_{\text{treatment}} - \text{absorbance}_{\text{positive control}})/(\text{absorbance}_{\text{negative control}} - \text{absorbance}_{\text{positive control}}) \times 100\%$.

***In Vivo* Intracellular Antibody Delivery from Fluorous Nanoemulsions.** All animal studies were performed in compliance with the U.S. Department of Health and Human Services Guide for the Care and Use of Laboratory Animals and after approval by The Pennsylvania State University Institutional Animal Care and Use Committee. Bitransgenic (5−7 week old) Inv-tTA × tetOHRas^{G12V} mice on a suppressive doxycycline dose in drinking water were shaved on their dorsal surface and placed on a reduced doxycycline dose to induce epidermal squamous papillomas as previously described.[56] Treatment of NE$_{IgG}$ (1000:1 PFNA/Cy5.5-IgG molar ratio) in 0.1% saline was administered *via* retro-orbital injection to the InvRas mice ($n = 2$) at 3 weeks postinduction ($t = 0$). Ultrasound activation of the particles was performed using a Nepagene Sonitron GTS with a plane wave transducer (1 MHz, 6 mm diameter). Ultrasound gel and the transducer were applied directly on top of the tumor of interest. Tumors were multiply activated with ultrasound (2.0 W/cm^2, 20% duty cycle, 90 s) at $t = 2$ h, 6 h, 24 h, and 5 days with mice sacrificed after the final insonation. Both control tumors (+NE$_{IgG}$, −US) and multiactivated tumors (+NE$_{IgG}$, +US) were harvested at day 5 and cyro-sectioned. To visualize IgG intracellular delivery, tissue sections were stained using streptavidin−biotin immunofluorescence. Sections were rehydrated in PBS, blocked for endogenous biotin using Vector Laboratories avidin/biotin blocking kit (following manufacturer instructions), and then blocked with 5% goat serum in PBS for 40 min. Section were then incubated with a biotinylated goat anti-rabbit IgG antibody (1:500) in BSA/PBS for 1 h. Bound antibody was localized using streptavidin-AlexaFluor488 (1:500) in BSA/PBS. Propidium iodide (PI) was used to localize nuclei of tumor cells. All staining was performed at room temperature. Each tumor section (control and multiple activated) had a corresponding internal control sample to assess nonspecific binding of streptavidin-AlexaFluor488. Sections were imaged on an Olympus Fluoview 1000 confocal microscope with a PlanApo 40×/1.4 oil objective lens using 488 and 543 nm single photon lasers for AlexaFluor488 and PI signals, respectively. Relative intracellular fluorescence was semiquantitatively analyzed *via* ImageJ. Calculated average fluorescence per cell was normalized by an internal control, shown as mean ± SEM for $n = 100$ cells per condition.

Ultrasound B-Mode and Doppler Imaging. To prepare tissue phantoms, a solution of 1.5 w/v% agarose was degassed and allowed to gelate into a cylindrical mold using a 50 mL beaker. During gelation, a 1 cm diameter glass tube was inserted to create a ∼2 cm deep sample cavity. NE$_{GFP}$ emulsions were prepared at a 1:10 dilution of the stock into degassed DI water and then loaded into the gel cavity. The agarose phantom was then placed on top of an acoustically absorbing neoprene block and partially submerged in a tank of degassed water to allow for acoustic imaging. NE$_{GFP}$ emulsions were imaged in B-mode and Doppler using an L22-14v (18.5 MHz, 12 cycles) and L7-4 (5 MHz, 3 cycles) transducer, respectively. Using a Verasonics research ultrasound system, the voltage sent to the transducers was incrementally increased for image-guided particle tracking in B-mode and for acoustic droplet vaporization *via* the Doppler mode. Video images were captured and in-phase quadrature (I/Q) Doppler data saved at discrete time points. Acoustic pressures were determined relative to applied transducer voltage using a golden capsule hydrophone (see Figure S16), and derated through ∼1 cm of an agarose phantom using an estimated attenuation coefficient of −0.5 dB/cm·MHz.[63] The inertial cavitation threshold of the emulsions was calculated from three independent experimental replicates.

ASSOCIATED CONTENT

Supporting Information

The Supporting Information is available free of charge at https://pubs.acs.org/doi/10.1021/acsnano.9b08745.

Table identifying the screened FTags, additional ^{19}F NMR spectra of fluorous compounds, GFP fluorescence from ultrasound exposure, FTag dispersion screening for IgG, NE$_{IgG}$ particles size, and treated tumor section micrographs, RP-HPLC and ESI-MS spectra of RGD-peptide, and 5 MHz ultrasound transducer acoustic pressure correlation (PDF)

Movie S1: B-mode ultrasound guidance of NE$_{GFP}$ nanoemulsions (MOV)

Movie S2: Doppler ultrasound imaging of NE$_{GFP}$ nanoemulsion cavitation (MOV)

AUTHOR INFORMATION

Corresponding Author

Scott H. Medina − *Department of Biomedical Engineering, The Pennsylvania State University, University Park, Pennsylvania 16802, United States;* orcid.org/0000-0001-5441-2164; Email: shm126@psu.edu

Authors

Janna N. Sloand − *Department of Biomedical Engineering, The Pennsylvania State University, University Park, Pennsylvania 16802, United States*

Theodore T. Nguyen − *Department of Veterinary and Biomedical Sciences, The Pennsylvania State University, University Park, Pennsylvania 16802, United States*

Scott A. Zinck − *Graduate Program in Acoustics, The Pennsylvania State University, University Park, Pennsylvania 16802, United States*

Erik C. Cook − *Department of Chemistry, The Pennsylvania State University, University Park, Pennsylvania 16802, United States*

Tawanda J. Zimudzi − *Materials Research Institute, The Pennsylvania State University, University Park, Pennsylvania 16802, United States;* orcid.org/0000-0001-7847-9646

Scott A. Showalter − *Department of Chemistry, The Pennsylvania State University, University Park, Pennsylvania 16802, United States;* orcid.org/0000-0001-5179-032X

Adam B. Glick − *Department of Veterinary and Biomedical Sciences, The Pennsylvania State University, University Park, Pennsylvania 16802, United States*

Julianna C. Simon − *Graduate Program in Acoustics, The Pennsylvania State University, University Park, Pennsylvania 16802, United States*

Complete contact information is available at:
https://pubs.acs.org/10.1021/acsnano.9b08745

Author Contributions

J.N.S. and S.H.M. conceived the hypothesis, designed the experiments, and wrote the manuscript. J.N.S., T.T.N., E.C.C., T.J.Z., and S.A.Z. designed and performed the experiments, analyzed the results, and contributed to writing of the manuscript. S.A.S., A.B.G., and J.C.S. contributed to the design of experiments.

Notes

The authors declare no competing financial interest.

ACKNOWLEDGMENTS

We acknowledge and thank the Penn State Microscopy and Cytometry Facility, University Park, PA, for assistance with confocal microscopy. We also acknowledge the Penn State X-ray Crystallography Facility, Materials Characterization Laboratory, and NMR Facility, University Park, PA, for use of the CD spectrophotometer, dynamic light scattering, and FTIR instrumentation and NMR spectrometers, respectively. We thank the laboratory of J. Schneider at the National Cancer Institute for providing green fluorescent protein and the A549 lung carcinoma cell line. We thank the laboratory of Y. Wang at Penn State University for providing the anti-β-tubulin antibody. Funding for this research was provided by the NSF Faculty Early Career Development Program (CAREER) to S.H.M. under Award No. DMR-1845053, and Penn State Institute of Energy and the Environment Human Health and the Environment Seed Grant awarded to A.B.G. Funds from the Penn State Graduate Research Fellowship supported J.N.S.

REFERENCES

(1) Lagassé, H. A. D.; Alexaki, A.; Simhadri, V. L.; Katagiri, N. H.; Jankowski, W.; Sauna, Z. E.; Kimchi-Sarfaty, C. Recent Advances in (Therapeutic Protein) Drug Development. *F1000Research* **2017**, *6*, 113.

(2) Leader, B.; Baca, Q. J.; Golan, D. E. Protein Therapeutics: A Summary and Pharmacological Classification. *Nat. Rev. Drug Discovery* **2008**, *7*, 21−39.

(3) Zhang, Y.; Yu, J.; Bomba, H. N.; Zhu, Y.; Gu, Z. Mechanical Force-Triggered Drug Delivery. *Chem. Rev.* **2016**, *116*, 12536−12563.

(4) Almeida, A. J.; Souto, E. Solid Lipid Nanoparticles as a Drug Delivery System for Peptides and Proteins. *Adv. Drug Delivery Rev.* **2007**, *59*, 478−490.

(5) Wang, M.; Alberti, K.; Sun, S.; Arellano, C. L.; Xu, Q. Combinatorially Designed Lipid-Like Nanoparticles for Intracellular Delivery of Cytotoxic Protein for Cancer Therapy. *Angew. Chem.* **2014**, *126*, 2937−2942.

(6) Zuris, J. A.; Thompson, D. B.; Shu, Y.; Guilinger, J. P.; Bessen, J. L.; Hu, J. H.; Maeder, M. L.; Joung, J. K.; Chen, Z.-Y.; Liu, D. R. Cationic Lipid-Mediated Delivery of Proteins Enables Efficient Protein-Based Genome Editing *In Vitro* and *In Vivo*. *Nat. Biotechnol.* **2015**, *33*, 73−80.

(7) Cheng, R.; Meng, F.; Deng, C.; Klok, H.-A.; Zhong, Z. Dual and Multi-Stimuli Responsive Polymeric Nanoparticles for Programmed Site-Specific Drug Delivery. *Biomaterials* **2013**, *34*, 3647−3657.

(8) Gu, Z.; Biswas, A.; Zhao, M.; Tang, Y. Tailoring Nanocarriers for Intracellular Protein Delivery. *Chem. Soc. Rev.* **2011**, *40*, 3638−3655.

(9) Yan, M.; Du, J.; Gu, Z.; Liang, M.; Hu, Y.; Zhang, W.; Priceman, S.; Wu, L.; Zhou, Z. H.; Liu, Z.; Segura, T.; Tang, Y.; Lu, Y. A Novel Intracellular Protein Delivery Platform Based on Single-Protein Nanocapsules. *Nat. Nanotechnol.* **2010**, *5*, 48−53.

(10) Shen, H.; Liu, M.; He, H.; Zhang, L.; Huang, J.; Chong, Y.; Dai, J.; Zhang, Z. PEGylated Graphene Oxide-Mediated Protein Delivery for Cell Function Regulation. *ACS Appl. Mater. Interfaces* **2012**, *4*, 6317−6323.

(11) Kavitha, T.; Kang, I.-K.; Park, S.-Y. Poly(Acrylic Acid)-Grafted Graphene Oxide as an Intracellular Protein Carrier. *Langmuir* **2014**, *30*, 402−409.

(12) Jiang, T.; Sun, W.; Zhu, Q.; Burns, N. A.; Khan, S. A.; Mo, R.; Gu, Z. Furin-Mediated Sequential Delivery of Anticancer Cytokine and Small-Molecule Drug Shuttled by Graphene. *Adv. Mater.* **2015**, *27*, 1021−1028.

(13) Chithrani, B. D.; Chan, W. C. W. Elucidating the Mechanism of Cellular Uptake and Removal of Protein-Coated Gold Nanoparticles of Different Sizes and Shapes. *Nano Lett.* **2007**, *7*, 1542−1550.

(14) Tang, R.; Jiang, Z.; Ray, M.; Hou, S.; Rotello, V. M. Cytosolic Delivery of Large Proteins Using Nanoparticle-Stabilized Nanocapsules. *Nanoscale* **2016**, *8*, 18038−18041.

(15) Lv, J.; Fan, Q.; Wang, H.; Cheng, Y. Polymers for Cytosolic Protein Delivery. *Biomaterials* **2019**, *218*, 119358.

(16) Fu, A.; Tang, R.; Hardie, J.; Farkas, M. E.; Rotello, V. M. Promises and Pitfalls of Intracellular Delivery of Proteins. *Bioconjugate Chem.* **2014**, *25*, 1602−1608.

(17) Lowe, K. C. Perfluorinated Blood Substitutes and Artificial Oxygen Carriers. *Blood Rev.* **1999**, *13*, 171−184.

(18) Squires, J. E. Artificial Blood. *Science* **2002**, *295*, 1002−1005.

(19) Castro, C. I.; Briceno, J. C. Perfluorocarbon-Based Oxygen Carriers: Review of Products and Trials. *Artif. Organs* **2010**, *34*, 622−634.

(20) O'Donnell, K. A.; Caty, M. G.; Zheng, S.; Rossman, J. E.; Azizkhan, R. G. Oxygenated Intraluminal Perfluorocarbon Protects Intestinal Muscosa from Ischemia/Reperfusion Injury. *J. Pediatr. Surg.* **1997**, *32*, 361−365.

(21) Fix, S. M.; Borden, M. A.; Dayton, P. A. Therapeutic Gas Delivery *via* Microbubbles and Liposomes. *J. Controlled Release* **2015**, *209*, 139−149.

(22) Bardin, D.; Martz, T. D.; Sheeran, P. S.; Shih, R.; Dayton, P. A.; Lee, A. P. High-Speed, Clinical-Scale Microfluidic Generation of Stable Phase-Change Droplets for Gas Embolotherapy. *Lab Chip* **2011**, *11*, 3990−3998.

(23) Samuel, S.; Duprey, A.; Fabiilli, M. L.; Bull, J. L.; Fowlkes, J. B. *In Vivo* Microscopy of Targeted Vessel Occlusion Employing Acoustic Droplet Vaporization. *Microcirculation* **2012**, *19*, 501−509.

(24) Rapoport, N. Drug-Loaded Perfluorocarbon Nanodroplets for Ultrasound-Mediated Drug Delivery. *Adv. Exp. Med. Biol.* **2016**, *880*, 221−241.

(25) Williams, R.; Wright, C.; Cherin, E.; Reznik, N.; Lee, M.; Gorelikov, I.; Foster, F. S.; Matsuura, N.; Burns, P. N. Characterization of Submicron Phase-Change Perfluorocarbon Droplets for Extravascular Ultrasound Imaging of Cancer. *Ultrasound Med. Biol.* **2013**, *39*, 475−489.

(26) Rapoport, N. Phase-Shift, Stimuli-Responsive Perfluorocarbon Nanodroplets for Drug Delivery to Cancer. *Wiley Interdiscip. Rev.: Nanomed. Nanobiotechnol.* **2012**, *4*, 492−510.

(27) Klibanov, A. L. Microbubble Contrast Agents: Targeted Ultrasound Imaging and Ultrasound-Assisted Drug-Delivery Applications. *Invest. Radiol.* **2006**, *41*, 354−362.

(28) Freire, M. G.; Carvalho, P. J.; Santos, L. M. N. B. F.; Gomes, L. R.; Marrucho, I. M.; Coutinho, J. A. P. Solubility of Water in Fluorocarbons: Experimental and COSMO-RS Prediction Results. *J. Chem. Thermodyn.* **2010**, *42*, 213−219.

(29) Kripfgans, O. D.; Fowlkes, J. B.; Miller, D. L.; Eldevik, O. P.; Carson, P. L. Acoustic Droplet Vaporization for Therapeutic and Diagnostic Applications. *Ultrasound Med. Biol.* **2000**, *26*, 1177−1189.

(30) Fabiilli, M. L.; Haworth, K. J.; Fakhri, N. H.; Kripfgans, O. D.; Carson, P. L.; Fowlkes, J. B. The Role of Inertial Cavitation in Acoustic Droplet Vaporization. *IEEE Trans. Ultrason. Eng.* **2009**, *56*, 1006−1017.

(31) Mura, S.; Nicolas, J.; Couvreur, P. Stimuli-Responsive Nanocarriers for Drug Delivery. *Nat. Mater.* **2013**, *12*, 991−1003.

(32) Fabiilli, M. L.; Lee, J. A.; Kripfgans, O. D.; Carson, P. L.; Fowlkes, J. B. Delivery of Water-Soluble Drugs Using Acoustically

Triggered Perfluorocarbon Double Emulsions. *Pharm. Res.* **2010**, *27*, 2753−2765.

(33) Duncanson, W. J.; Arriaga, L. R.; Ung, W. L.; Kopechek, J. A.; Porter, T. M.; Weitz, D. A. Microfluidic Fabrication of Perfluorohexane-Shelled Double Emulsions for Controlled Loading and Acoustic-Triggered Release of Hydrophilic Agents. *Langmuir* **2014**, *30*, 13765−13770.

(34) Chen, G.; Wang, K.; Wu, P.; Wang, Y.; Zhou, Z.; Yin, L.; Sun, M.; Oupický, D. Development of Fluorinated Polyplex Nanoemulsions for Improved Small Interfering RNA Delivery and Cancer Therapy. *Nano Res.* **2018**, *11*, 3746−3761.

(35) Gao, D.; Xu, M.; Cao, Z.; Gao, J.; Chen, Y.; Li, Y.; Yang, Z.; Xie, X.; Jiang, Q.; Wang, W.; Liu, J. Ultrasound-Triggered Phase-Transition Cationic Nanodroplets for Enhanced Gene Delivery. *ACS Appl. Mater. Interfaces* **2015**, *7*, 13524−13537.

(36) Geers, B.; Dewitte, H.; De Smedt, S. C.; Lentacker, I. Crucial Factors and Emerging Concepts in Ultrasound-Triggered Drug Delivery. *J. Controlled Release* **2012**, *164*, 248−255.

(37) Cavalli, R.; Bisazza, A.; Trotta, M.; Argenziano, M.; Civra, A.; Donalisio, M.; Lembo, D. New Chitosan Nanobubbles for Ultrasound-Mediated Gene Delivery: Preparation and *In Vitro* Characterization. *Int. J. Nanomed.* **2012**, *7*, 3309−3318.

(38) Hernot, S.; Klibanov, A. L. Microbubbles in Ultrasound-Triggered Drug and Gene Delivery. *Adv. Drug Delivery Rev.* **2008**, *60*, 1153−1166.

(39) Fan, Z.; Kumon, R. E.; Deng, C. X. Mechanisms of Microbubble-Facilitated Sonoporation for Drug and Gene Delivery. *Ther. Delivery* **2014**, *5*, 467−486.

(40) Tang, M.-X.; Mulvana, H.; Gauthier, T.; Lim, A. K. P.; Cosgrove, D. O.; Eckersley, R. J.; Stride, E. Quantitative Contrast-Enhanced Ultrasound Imaging: A Review of Sources of Variability. *Interface Focus* **2011**, *1*, 520−539.

(41) Martin, K. H.; Dayton, P. A. Current Status and Prospects for Microbubbles in Ultrasound Theranostics. *Wiley Interdiscip. Rev.: Nanomed. Nanobiotechnol.* **2013**, *5*, 329−345.

(42) Yang, W. J.; Neoh, K.-G.; Kang, E.-T.; Teo, S. L.-M.; Rittschof, D. Polymer Brush Coatings for Combating Marine Biofouling. *Prog. Polym. Sci.* **2014**, *39*, 1017−1042.

(43) Marabotti, I.; Morelli, A.; Orsini, L. M.; Martinelli, E.; Galli, G.; Chiellini, E.; Lien, E. M.; Pettitt, M. E.; Callow, M. E.; Callow, J. A.; Conlan, S. L.; Mutton, R. J.; Clare, A. S.; Kocijan, A.; Donik, C.; Jenko, M. Fluorinated/Siloxane Copolymer Blends for Fouling Release: Chemical Characterisation and Biological Evaluation with Algae and Barnacles. *Biofouling* **2009**, *25*, 481−493.

(44) Krishnan, S.; Weinman, C. J.; Ober, C. K. Advances in Polymers for Anti-Biofouling Surfaces. *J. Mater. Chem.* **2008**, *18*, 3405−3413.

(45) United States Food and Drug Administration. Rules and Regulations, Part 173: Secondary direct food additives permitted in food for human consumption Part 173, Authority: 21 USC, 321, 342, 348. *Federal Register* 2001, *66*, 123.

(46) Waldo, G. S.; Standish, B. M.; Berendzen, J.; Terwilliger, T. C. Rapid Protein-Folding Assay Using Green Fluorescent Protein. *Nat. Biotechnol.* **1999**, *17*, 691−695.

(47) Sheeran, P. S.; Luois, S. H.; Mullin, L. B.; Matsunaga, T. O.; Dayton, P. A. Design of Ultrasonically-Activatable Nanoparticles Using Low Boiling Point Perfluorocarbons. *Biomaterials* **2012**, *33*, 3262−3269.

(48) Nie, B.; Stutzman, J.; Xie, A. A Vibrational Spectral Maker for Probing the Hydrogen-Bonding Status of Protonated Asp and Glu Residues. *Biophys. J.* **2005**, *88*, 2833−2847.

(49) Medina, S. H.; Michie, M. S.; Miller, S. E.; Schnermann, M. J.; Schneider, J. P. Fluorous Phase-Directed Peptide Assembly Affords Nano-Peptisomes Capable of Ultrasound-Triggered Cellular Delivery. *Angew. Chem., Int. Ed.* **2017**, *56*, 11404−11408.

(50) Brennen, C. E. *Fundamentals of Multiphase Flow*; Cambridge University Press: Cambridge, UK, 2005; pp 128−149.

(51) Leighton, T. *The Acoustic Bubble*; Academic Press: San Diego, CA, 2012; pp 67−128.

(52) Brennen, C. E. *Cavitation and Bubble Dynamics*; Cambridge University Press: Cambridge, UK, 2013.

(53) Lentacker, I.; De Cock, I.; Deckers, R.; De Smedt, S. C.; Moonen, C. T. W. Understanding Ultrasound Induced Sonoporation: Definitions and Underlying Mechanisms. *Adv. Drug Delivery Rev.* **2014**, *72*, 49−64.

(54) Shang, L.; Nienhaus, K.; Nienhaus, G. U. Engineered Nanoparticles Interacting with Cells: Size Matters. *J. Nanobiotechnol.* **2014**, *12*, 5−5.

(55) He, C.; Hu, Y.; Yin, L.; Tang, C.; Yin, C. Effects of Particle Size and Surface Charge on Cellular Uptake and Biodistribution of Polymeric Nanoparticles. *Biomaterials* **2010**, *31*, 3657−3666.

(56) Podolsky, M. A.; Bailey, J. T.; Gunderson, A. J.; Oakes, C. J.; Breech, K.; Glick, A. B. Differentiated State of Initiating Tumor Cells is Key to Distinctive Immune Responses Seen in H-RasG12V-Induced Squamous Tumors. *Cancer Immunol. Res.* **2017**, *5*, 198−210.

(57) Oeffinger, B. E.; Wheatley, M. A. Development and Characterization of a Nano-Scale Contrast Agent. *Ultrasonics* **2004**, *42*, 343−347.

(58) Matsunaga, T. O.; Sheeran, P. S.; Luois, S.; Streeter, J. E.; Mullin, L. B.; Banerjee, B.; Dayton, P. A. Phase-Change Nanoparticles Using Highly Volatile Perfluorocarbons: Toward a Platform for Extravascular Ultrasound Imaging. *Theranostics* **2012**, *2*, 1185−1198.

(59) Zhou, Y.; Shi, J.; Cui, J.; Deng, C. X. Effects of Extracellular Calcium on Cell Membrane Resealing in Sonoporation. *J. Controlled Release* **2008**, *126*, 34−43.

(60) Zhou, Y.; Kumon, R. E.; Cui, J.; Deng, C. X. The Size of Sonoporation Pores on the Cell Membrane. *Ultrasound Med. Biol.* **2009**, *35*, 1756−1760.

(61) Zhang, Z.; Shen, W.; Ling, J.; Yan, Y.; Hu, J.; Cheng, Y. The Fluorination Effect of Fluoroamphiphiles in Cytosolic Protein Delivery. *Nat. Commun.* **2018**, *9*, 1377.

(62) Lv, J.; He, B.; Yu, J.; Wang, Y.; Wang, C.; Zhang, S.; Wang, H.; Hu, J.; Zhang, Q.; Cheng, Y. Fluoropolymers for Intracellular and *In Vivo* Protein Delivery. *Biomaterials* **2018**, *182*, 167−175.

(63) Browne, J.; Ramnarine, K.; Watson, A.; Hoskins, P. Assessment of the Acoustic Properties of Common Tissue-Mimicking Test Phantoms. *Ultrasound Med. Biol.* **2003**, *29*, 1053−1060.